Article

Dynamic Jahn-Teller effect in the strong spin-orbit coupling regime

Ivica Živković [1] ✉, Jian-Rui Soh [1], Oleg Malanyuk[1], Ravi Yadav [1], Federico Pisani [1], Aria M. Tehrani[2], Davor Tolj[1], Jana Pasztorova[1], Daigorou Hirai [3], Yuan Wei[4], Wenliang Zhang [4], Carlos Galdino[4], Tianlun Yu[4], Kenji Ishii [5], Albin Demuer[6], Oleg V. Yazyev [7], Thorsten Schmitt [4] & Henrik M. Rønnow [1]

Exotic quantum phases, arising from a complex interplay of charge, spin, lattice and orbital degrees of freedom, are of immense interest to a wide research community. A well-known example of such an entangled behavior is the Jahn-Teller effect, where the lifting of orbital degeneracy proceeds through lattice distortions. Here we demonstrate that a highly-symmetrical $5d^1$ double perovskite Ba_2MgReO_6, comprising a 3D array of isolated ReO_6 octahedra, represents a rare example of a dynamic Jahn-Teller system in the strong spin-orbit coupling regime. Thermodynamic and resonant inelastic x-ray scattering experiments, supported by quantum chemistry calculations, undoubtedly show that the Jahn-Teller instability leads to a ground-state doublet, resolving a long-standing puzzle in this family of compounds. The dynamic state of ReO_6 octahedra persists down to the lowest temperatures, where a multipolar order sets in, allowing for investigations of the interplay between a dynamic JT effect and strongly correlated electron behavior.

The importance of the Jahn-Teller (JT) effect reaches across many areas of chemistry, physics, and applied sciences[1]. Examples range from localized systems like photo-excited methane cations[2,3], ultra-fast transients in molecular complexes[4], and vacancy diffusion in graphene[5] towards more cooperative phenomena, including high-temperature superconductivity in cuprates[6], colossal magneto-resistance in manganites[7], metal-insulator transition in ruthenates[8] and antiferroelectricity in lacunar spinels[9]. The cornerstone of the JT effect is the existence of an electronic state with orbital degeneracy, leading to an overall decrease in the energy once the degeneracy is lifted. Typically, this occurs through ligand (L) displacement, which consequently affects both the electronic and magnetic properties of materials. In strongly correlated systems, where ligands are shared between neighboring metal (M) sites, the distortions at one site are correlated with distortions on neighboring sites, leading to a cooperative JT effect[10].

In the case of isolated, highly symmetric clusters, the system can choose among equivalent directions of distortion, resulting in a potential energy surface (PES) with multiple valleys and energy barriers between them. In the simplest case of an ML_6 octahedron having a single electron or a hole in a doubly-degenerate orbital state (well-known cases are Mn^{3+} and Cu^{2+} ions), the distortion can freeze along principal axes x, y, and z, producing a static JT effect. If the barriers are small enough so that the wave function is distributed over all valleys equally, the vibronic symmetry is restored, resulting in a dynamic JT effect. Many aspects of solid-state physics have been theoretically investigated through the coupling to continuous symmetries in JT systems[11–13], but the available materials are rather scarce. The inter-

[1]Laboratory for Quantum Magnetism, Institute of Physics, École Polytechnique Fédérale de Lausanne, Lausanne, Switzerland. [2]Department of Materials, ETH Zurich, Zurich, Switzerland. [3]Department of Applied Physics, Nagoya University, Nagoya, Japan. [4]Paul Scherrer Institute, Villigen PSI, Switzerland. [5]Synchrotron Radiation Research Center, National Institutes for Quantum Science and Technology, Sayo, Hyogo, Japan. [6]Université Grenoble Alpes, INSA Toulouse, Université Toulouse Paul Sabatier, CNRS, LNCMI, Grenoble, France. [7]Chair of Computational Condensed Matter Physics, Institute of Physics, École Polytechnique Fédérale de Lausanne, Lausanne, Switzerland. ✉e-mail: ivica.zivkovic@epfl.ch

cluster interaction needs to be very small to avoid a cooperative JT effect, while other couplings, like exchange interactions, should remain appreciable. Examples of materials where a dynamic JT effect has been suggested to occur include an unconventional molecular superconductor Cs_3C_{60}, where, together with Mott localization, it drives the material across a metal-to-insulator transition[14–16]. It has also been argued that the observed permittivity[17] in a paraelectric phase of $BaTiO_3$ stems from the resonating state between minima of the PES, which, under the influence of an electric field, become nonequivalent and trap Ti ions along one direction[18]. Eventually, the dynamic JT effect is overcome by the interaction between the centers, leading to a ferroelectric phase transition.

These examples involve relatively light elements, including $3d$ transition metal cations, where the influence of spin-orbit coupling (SOC) is considered negligible. Recently, a growing interest has been devoted to strong SOC systems, encompassing topological insulators[19], Dirac and Weyl semimetals[20], and Kitaev spin liquids[21]. The JT effect, on the other hand, has seldom been investigated in the context of strong SOC, with several examples devoted to Ir^{4+} systems[22,23]. Some $4f$ systems have been investigated before, like PrO_2[24], where the crystal field effect is much weaker compared to compounds based on d orbitals. More generally, a strong SOC qualitatively changes the ground-state wave functions and has been

proposed to renormalize the associated distortion, or even completely remove it above a certain critical value[25].

In this study, we present compelling evidence that Ba_2MgReO_6, a member of the $5d^1$ double-perovskite family, displays a distinctive set of properties that make it exceptionally well-suited for the exploration of the role of the dynamic JT effect on strongly correlated electrons in the presence of a strong SOC. This is promoted by a high-symmetry environment of Re^{6+} ions, covalently coupled to six oxygen ions, alternating with ionic Mg^{2+} ions and forming a three-dimensional array of nearly-independent, JT-active ReO_6 octahedra, Fig. 1a. Strong SOC mixes the t_{2g} levels into a $j_{eff} = 3/2$ quartet and a $j_{eff} = 1/2$ doublet, separated by Δ_{SO}, as shown in Fig. 1b. The JT instability manifests itself as the splitting of the ground-state quartet into two doublets, with the gap Δ_{JT} directly related to the amplitude of the distortion. The correlated nature of $5d$ electrons is reflected in the formation of a multipolar order[26,27], encompassing a charge quadrupole state below $T_Q = 33$ K and a magnetic dipole state below $T_M = 18$ K (Fig. 1c, d).

Using spectroscopic and thermodynamic evidence, we show that the JT instability causes the doublet-doublet splitting in Ba_2MgReO_6 at temperatures $T >> T_M$, T_Q. We quantify the associated distortions through local cluster calculations and determine that the energy barriers between the local minima are smaller than the zero-point motion energy, establishing Ba_2MgReO_6 as a dynamic JT system. Additionally,
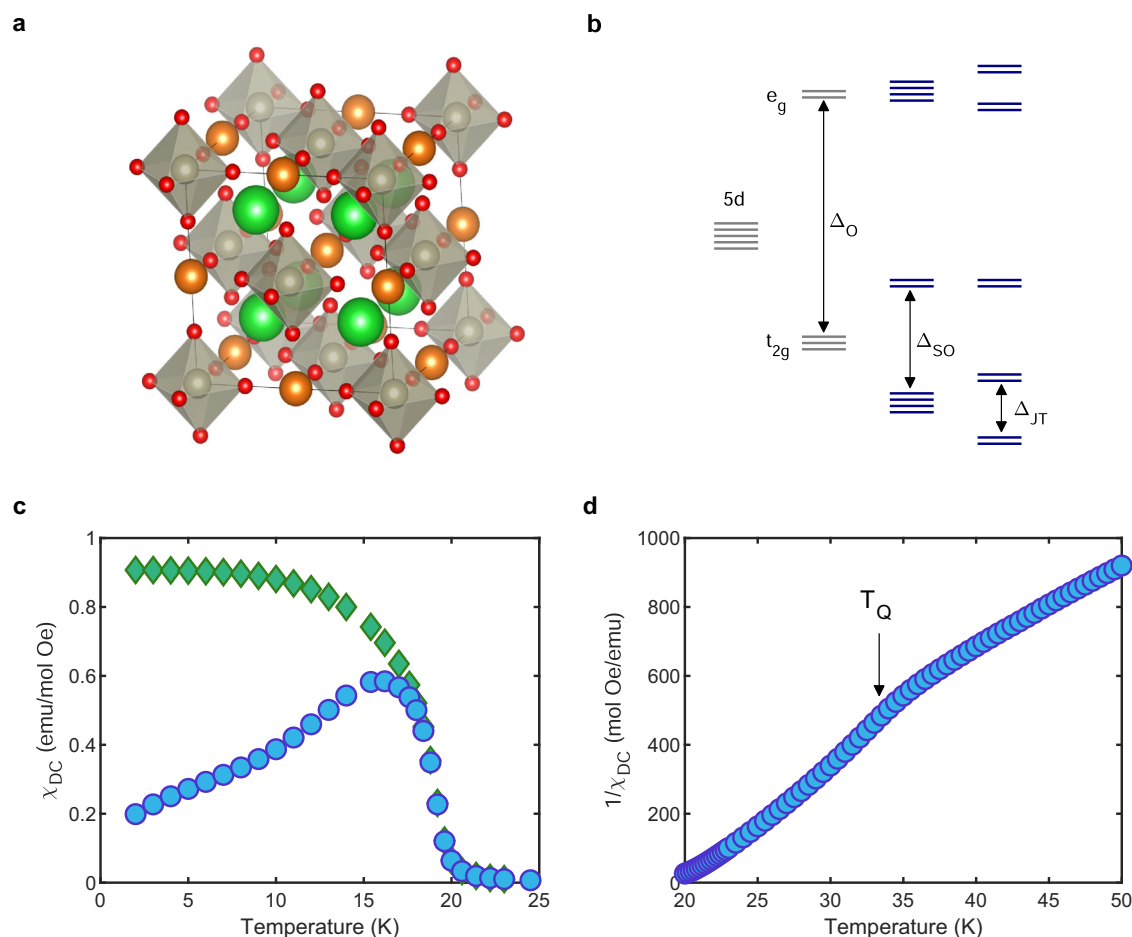
Fig. 1 | The crystal environment of Ba_2MgReO_6 and the multipolar order. a The unit cell of Ba_2MgReO_6 with semi-transparent ReO_6 octahedra and red circles representing oxygen ions. Mg and Ba ions are represented by orange and green circles, respectively. **b** Schematic representation of the splitting of Re $5d$-levels under the influence of crystal field (Δ_O), spin-orbit coupling (Δ_{SO}), and a JT effect (Δ_{JT}). Light gray lines represent orbitals, each allowing for two spin states. Dark blue

lines represent SOC-entangled states. **c** T-dependence of dc magnetic susceptibility measured with $B = 0.1$ T after zero-field-cooled (blue circles) and field-cooled (green diamonds) protocols. The transition temperature into long-range magnetic order occurs at $T_M = 18$ K and is marked by the splitting of two curves. **d** T-dependence of the inverse susceptibility with the temperature of the quadrupolar order T_Q indicated as a change of the slope.
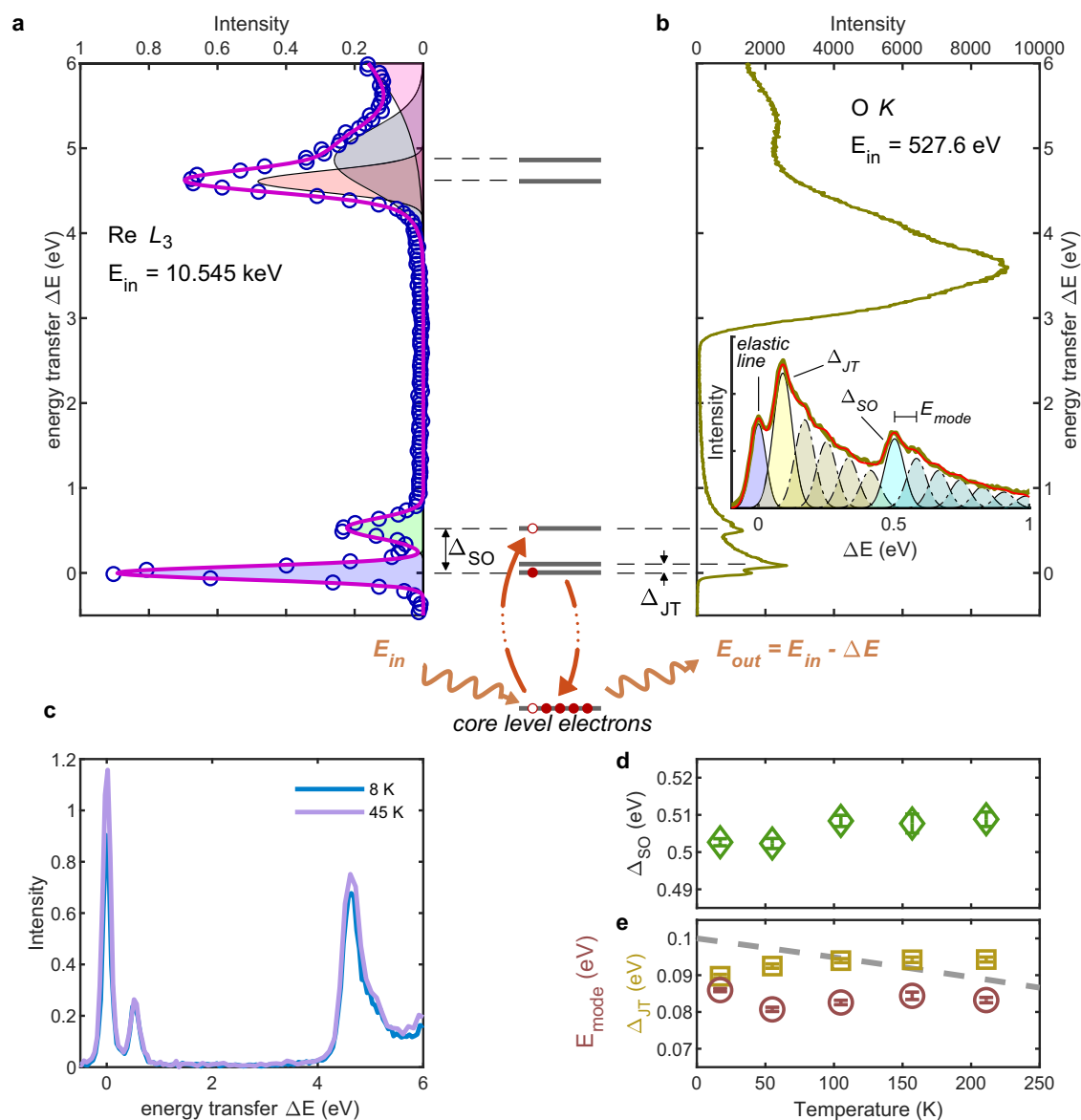
Fig. 2 | Resonant inelastic x-ray scattering on Ba$_2$MgReO$_6$. a RIXS spectra at the Re L_3 edge. The full purple line represents a sum of Gaussian contributions (shaded areas with black lines) centered around the positions of localized $5d$ Re levels (gray lines between panels (**a**) and (**b**)). **b** RIXS spectra at the O K edge. The excitations below 1 eV correspond to localized $d − d$ processes, while the broad features above 2.8 eV arise from fluorescence. The inset shows an expanded region below 1 eV with highlighted contributions from individual modes. The cascade of modes above Δ_{JT} and Δ_{SO} is indicated by shaded areas with broken lines. The RIXS scattering involves a virtual process of core-level electron excitation with a photon of energy E_{in} while the outgoing photon's energy E_{out} is reduced by the energy difference ΔE, measuring the position of higher-lying d-levels. **c** Re RIXS spectra below and above T_Q. **d** T-dependence of Δ_{SO}. **e** T-dependence of Δ_{JT} and E_{mode}. The dashed line represents a hypothetic mean-field order parameter behavior $\Delta_{JT} \sim \sqrt{1 − T/T_{JT}}$ with $T_{JT} = 1000$ K. The error bars are given as one standard deviation obtained from the fit.

through a careful analysis of specific heat results, we establish that the total entropy across both transitions reaches only $R2$.

Results

Local d-d excitations

To probe the localized states of Re ions, we employ resonant inelastic x-ray scattering (RIXS). In Fig. 2a, we display the low temperature ($T = 8$ K) energy dependence of the scattering intensity obtained at the Re L_3 edge, displaying multiple peaks of varying widths, which we assign as follows (see also the Supplementary Material). The peak around zero energy is an elastic line, where no energy transfer occurs during the virtual excitation of core-level electrons. Further peaks reflect virtual processes where core-level electrons are excited to unoccupied states while the recombination of the core-level hole

occurs with electrons on occupied Re $5d$ states. We find that the observed scattering intensity profile can be fully described by assuming that each peak is represented by a simple Gaussian contribution. The positions of maxima correspond to crystal field levels of Re $5d$-orbitals and can be readily assigned following the scheme presented in Fig. 1b. The first peak at $\Delta E > 0$ represents the SOC-induced splitting between the ground state quartet and the higher-lying doublet state $\Delta_{SO} \cong 0.5$ eV which allows the estimate of the SOC constant $\lambda \sim 335$ meV. Up to 4 eV, the line shape is featureless, with two additional peaks present around 4.5–5 eV. A notable tail coming from an even higher-lying peak can be observed, which can be assigned to virtual processes involving the recombination with electrons originating from lower-lying, predominantly oxygen p-orbitals, located ~ 6.3 eV below the elastic line. A recent report[28] focusing on the

comparison between Ba_2MgReO_6, Sr_2MgReO_6, and Ca_2MgReO_6 found a slightly asymmetric line-shape around Δ_{SO}, ascribing it to the influence of phonon modes on spin-orbit excitations. Nevertheless, their value for Δ_{SO} in Ba_2MgReO_6, as well as the energies of higher-lying excitations, are in excellent agreement with our results.

The two peaks, situated at 4.7 eV and 4.9 eV, can be assigned to states belonging to e_g orbitals, with four-fold degeneracy being split into two doublets, in accordance with the JT scenario. An equivalent split of the ground state quartet is expected but not directly observed due to an insufficient energy resolution (~100 meV) of the experimental setup at the Re L_3 edge. On the other hand, the results obtained at the O K edge (Fig. 2b), with its ~50 meV resolution, show an additional peak at low energies reflecting the doublet-doublet splitting $\Delta_{JT} \cong 88$ meV. A similar finding has been reported very recently[29] for the sister compound Ba_2NaOsO_6, with the corresponding excitation at 95 meV. It is interesting to note that both experiments at the O K edge resulted in a similarly asymmetric line shape around Δ_{JT} and Δ_{SO}, with possible faint features on the high-energy side. The description of those features has recently been attempted in terms of coupling of phonon modes with spin-orbit excitations[28], although the asymmetry itself is still not fully understood. It is clear that several additional modes are necessary to describe such an asymmetric line shape, but if all the parameters are left independent, it quickly becomes unfeasible to perform the fitting procedure (see the Supplementary Material for more details). The approach we used is to model the high-energy tail of each $d - d$ excitation through a set of n dependent modes, whose energies and amplitudes are determined by simple relations, $E_n^\alpha = E_\alpha + n \cdot E_{mode}$ and $A_n^\alpha = A_0^\alpha e^{-n \cdot B}$, with all the additional modes having the same width. Here α stands for a JT or SO $d - d$ excitation (indicated by light colors in the inset of Fig. 2b), while additional modes are indicated by darker colors. Such an approach significantly reduces the number of independent parameters and leads to a very satisfactory description of the observed line shape within the relevant energy range up to 1 eV.

The central result of RIXS experiments comes from the temperature evolution of the acquired spectra. In Fig. 2c, we compare the Re L_3 RIXS spectra above and below T_M and T_Q. Within the resolution, there is no visible variation between the two line profiles. Specifically, the asymmetric shape at 4.5–5 eV, associated with the splitting of e_g orbitals, remains clearly unaffected. A more direct and profound evidence comes from $\Delta_{SO}(T)$ and $\Delta_{JT}(T)$, extracted from O K RIXS spectra and plotted in Panels 2d, e. Both are practically T-independent, with a small decrease of Δ_{JT} below T_Q.

It is not surprising that Δ_{SO} shows very little temperature dependence. On the contrary, the persistence of Δ_{JT} well above 200 K goes against the prevailing idea that the splitting of the ground-state quartet is linked with the appearance of the quadrupolar order at T_Q[30,31]. Moreover, we can infer that $\Delta_{JT} > 0$ to much higher temperatures since any order-parameter-like decrease would be readily observed in our data, as indicated in Fig. 2e by a dashed line.

Potential energy surface and the Jahn-Teller effect

Now we turn our efforts to characterize the type of distortion that accompanies the observed splitting. The relevant modes of an ML_6 octahedron are sketched in Fig. 3a–c. The magnitude of the isotropic mode mainly determines the octahedral splitting Δ_O which for Ba_2MgReO_6 is large enough to disregard the $t_{2g} - e_g$ mixing. Two other modes are JT-active, with Q_3 representing a tetragonal distortion while Q_2 describes the orthorhombic mode. For an isolated octahedron, with a linear coupling and in the limit of very small distortions, the PES is characterized by an infinite-degeneracy line, the so-called 'Mexican hat' potential (Fig. 3d). The octahedron remains dynamic, exploring all possible linear combinations in the $Q_2 - Q_3$ parameter space, with $\Delta_{JT} = const. > 0$. Increasing the amplitude of distortions leads to anharmonic effects and, together with

the presence of surrounding charges, breaks the line degeneracy, resulting in a multi-valley PES. An opposing effect has been argued to arise from strong SOC[25], driving the PES back towards a Mexican-hat potential but also suppressing the JT distortion, as well as reducing the energy gain due to the JT effect.

For a more quantitative insight, we perform embedding multi-reference quantum chemistry calculations taking into account SOC (see "Methods"). We start from the experimentally established structure at 40 K[27] and calculate the PES of the ReO_6 octahedron by parameterizing ligand displacements in terms of the above-described modes for a general distortion $\boldsymbol{\tau} = \alpha\boldsymbol{Q}_{iso} + \beta\boldsymbol{Q}_3 + \gamma\boldsymbol{Q}_2$. In Fig. 3e, we show the calculated PES exhibiting three valleys, corresponding to tetragonal distortions along the three principal axes. One of the minima is given by $\alpha \approx -1\%$, $\beta \approx -1.5\%$, and $\gamma = 0$, where $\beta < 0$ indicates that the degeneracy lifting of the ground-state quartet occurs through a contraction of the $Re - O_{apical}$ distance. A similar result has been obtained for Ba_2NaOsO_6[29], while calculations performed for a $4d^1$ compound Ba_2YMoO_6 indicate the same sign and a similar magnitude of distortions[32], thus establishing a clear tendency of d^1 octahedral systems towards a contraction, regardless of the strength of SOC. Importantly, both the sign and the magnitude of the calculated JT distortion are in stark contrast with the reported shift of oxygen ions below T_Q[27]. Detailed synchrotron x-ray diffraction analysis revealed[27] the lowering of the global symmetry from a cubic $Fm\overline{3}m$ above T_Q to a tetragonal $P4_2/mnm$ below T_Q, with a tetragonal elongation amounting to ~0.1% at low temperatures. This separation of scales undoubtedly disentangles the formation of the quadrupolar order at T_Q from the dominant, JT-induced splitting of the presumed ground-state quartet[30,33,34].

The validity of the performed calculations can be assessed by comparing the calculated energy levels with experimental data, as listed in Table 1. The calculations for the experimentally established structure at 40 K and the isotropically contracted one contain undistorted octahedra, resulting in $\Delta_{JT} = 0$ as well as four-fold degenerate e_g states (see Fig. 1). The calculations for distortions characterizing the minimum of a valley lead to $\Delta_{JT} = 78$ meV and the splitting of e_g states, a hallmark of the JT effect. All the calculated observables are found to be in the range of 10−20 % from the experimental values.

The minimum of the PES does not directly reflect the amplitude of the distortion of an octahedron. We use the calculated PES to obtain the wave function Ψ of the quantum-mechanical oscillator and its ground-state energy E_0. As shown in Fig. 3e, the wave function reflects the three-fold symmetry of the PES, extending towards each valley but still maintaining the absolute maximum at the center of the PES. More importantly, the energy $E_0 \approx 56$ meV is found well above the barrier between valleys $E_B \approx 35$ meV (Fig. 3f), implying that the zero-point motion prevents the freezing of vibronic degrees of freedom, which leaves each octahedron in a dynamic state. The characteristic time is typically expressed in the form $(t_0)^{-1} = (E_1 - E_0)/h$, where $E_1 \approx 102$ meV is the first excited state[35]. With $t_0 \approx 9 \cdot 10^{-14}$ s, only the scattering processes of x-rays and neutrons are fast enough to observe an instantaneous state of the system, all other experimental techniques obtain a dynamically averaged response.

We can calculate the probability distribution of Δ_{JT} using $S(\Delta_{JT}) = \int \Delta_{JT}(Q_i)|\Psi(Q_i)|^2 dQ_i$, where dQ_i designates an integration over the $Q_2 - Q_3$ space. The result presented in Fig. 3g reveals an asymmetric shape with a maximum occurring around 60 meV. We should emphasize that despite numerous approximations that underlie calculations, the results are directly comparable to experimentally obtained values. For comparison, the last column in Table 1 contains the results for a fictitious tetragonal $I4/mmm$ structure, where a small 0.15 % tetragonal elongation is implemented to reflect the observed cubic-to-tetragonal transition at T_Q[27]. The calculated Δ_{JT} is two orders of magnitude too small, unambiguously assigning the observed doublet-doublet splitting to a JT instability.
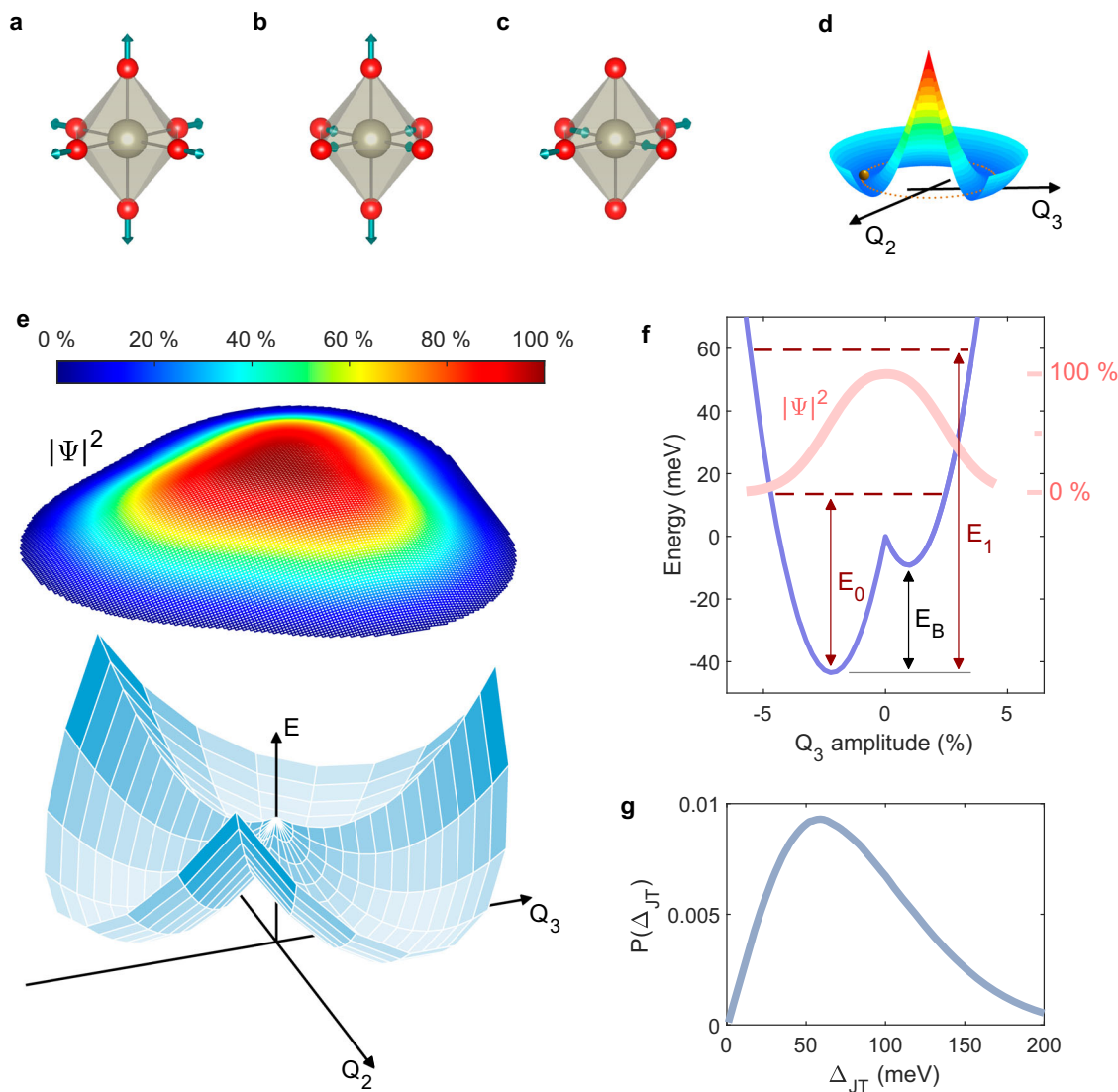
Fig. 3 | Vibrational modes and potential energy surface for a ReO₆ cluster. Definition of displacement modes: (**a**) isotropic mode $Q_{iso} = (1, 1, 1)$, (**b**) $Q_3 = (-\frac{1}{2}, -\frac{1}{2}, 1)$ and (**c**) $Q_2 = (-1, 1, 0)$. **d** A Mexican-hat potential with an infinite line degeneracy. **e** The PES was obtained using quantum chemistry calculations. Superimposed on top is the numerically calculated probability density $|\Psi|^2$ of the ground-state wave function $\Psi(E = E_0)$ with a cut-off at 20 % of the maximum value. **f** A cross-section of the PES for $Q_2 = 0$. **g** A probability distribution of Δ_{JT} calculated from $P(\Delta_{JT}) = \int \Delta_{JT}(Q_i)|\Psi(Q_i)|^2 dQ_i$.

These results can be naturally extended to other members of the double perovskite family, where bonding with ligands alternates regularly between an ionic and a covalent type. Many similarities exist with Ba_2NaOsO_6, which exhibits much smaller $T_M = 7.5$ K and $T_Q = 9.5$ K[31,36,37]. Another example is Cs_2TaCl_6, where a tetragonal contraction of $< 1\%$ has also been associated with the quadrupolar order[38], although a later single crystal study indicated a different value for T_Q[39]. Several d^2 compounds seem to retain high local symmetry[40], as well as a d^3 Ba_2YOsO_6 system[41], offering a variety of configurations where the interplay of a (dynamic) JT effect and strong SOC can be tested[25].

Entropy and the ground state doublet

The JT-splitting of the ground-state quartet has profound consequences for the thermodynamic properties of $5d^1$ systems. Already, the first report on Ba_2NaOsO_6 indicated a 'missing entropy'[36], extracted from electronic specific heat (C_{el}) measurements $S_{el} = \int (C_{el}/T)dT$ reaches only $\lesssim R2$, significantly smaller than the expected $R4$. Namely, the total recovered entropy is expected to reflect the ground-state degeneracy at high temperatures, released across two successive transitions T_M and T_Q, each contributing one $R2$[30,33,34]. Experimentally,

the main uncertainty comes from the determination of a proper phonon background, which leads to a wide array of recovered values of S_{el}[26,37,42–44]. We approach the problem of the phonon background determination by measuring specific heat C_P in magnetic fields, which, by affecting the electronic levels, causes a redistribution of measured C_P. Since the g-factor is strongly renormalized due to the partial cancellation of spin and orbital moments[30], it is necessary to apply large magnetic fields to see those effects around T_Q and above. In Fig. 4c, we plot the $C_P(T)$ of Ba_2MgReO_6 in magnetic fields up to 35 T. For $B = 0$, a sharp peak is seen at T_M and a broad shoulder around T_Q, in agreement with previously published results[26,44]. For $B = 35$ T, a broad feature is seen around T_Q, with the tail merging with $C_P(B = 0$ T) above ~45 K. We take this as an estimate up to which temperature the electronic contribution is appreciable and consider only the phonon contribution above it. Instead of an analytical form, we aim to utilize the results of first-principle calculations, which were recently used as an approximate description of the phonon specific heat in Ba_2MgReO_6[44]. We use a functional rescaling of the calculated results along both T − and C_P − axes to match the experimental data in the range 60–100 K (see the Supplementary Material for more details). The result of this

Table 1 | Calculated energy levels for various structures

(meV)	$Fm\bar{3}m$ @ 40 K	isotropic contraction (− 1%)	global minimum	EXP	I_4/mmm
Δ_{JT}	0	0	78	**88**	1
Δ_{SO}	560	561	606	**528**	584
Δ_O	5490	5573	5577	**4608**	5512
			5962	**4861**	5523

JT-distorted octahedra are characterized by a non-zero value of Δ_{JT} and two values for Δ_O. Columns refer to (from left to right): experimentally obtained ion positions at 40 K; ion positions after a 1% isotropic contraction of ReO_6 octahedron; ion positions at the global minima, which includes the amplitude of the Q_3 mode of −1.5%; (bold) experimental values obtained from Fig. 2; a fictitious tetragonal structure with 0.15% elongation.

procedure is presented in Fig. 4a as a black line, with the relative discrepancy remaining below 0.5% across the relevant range (see Fig. 4b).

The electronic contribution C_{el} extracted in this manner is displayed in Fig. 4c. Both features at T_M and T_Q are more clearly seen, as well as the magnetic field dependence. Initially T_M becomes rounded and shifts to higher temperatures, while there is very little effect on T_Q. With $B = 35$ T, however, we see the two features practically merged, with a sharp high-temperature tail. Qualitatively similar behavior has been observed in CeB_6[45,46] and assigned to field-induced octupolar moments on Ce ions[47,48]. Similarly, the NMR study[31] revealed a shift to higher temperatures of the order-disorder boundary in Ba_2NaOsO_6.

The total electronic entropy S_{el} extracted from Fig. 4c is presented in Fig. 4d. Within an error, the recovered values for all magnetic fields saturate very close to $R2$, with very little change above 40 K. This result is rather robust against small changes of the exact functional form of the phonon background and therefore, together with spectroscopic evidence obtained by RIXS and supported by quantum chemistry calculations, unequivocally establishes that the low energy physics in Ba_2MgReO_6 is dominated by a ground state doublet. A similar conclusion has been reached by a recent study on Ba_2NaOsO_6 where a somewhat larger doublet-doublet splitting has been found (95 meV) based on O K edge RIXS and x-ray magnetic circular dichroism[29]. We note that these two $5d^1$ systems exhibit qualitatively very similar behavior in terms of multi-polar ordering tendencies, with the advantage that Re^{6+} orders at sufficiently larger temperatures than Os^{7+} to allow a better insight into the peculiar interplay between magnetic dipole and charge quadrupole orders.

Discussion

The calculated ground-state energy suggests a dynamic type of distortion, where ReO_6 octahedra fluctuate with ~10 THz between elongations along three equivalent principal axes. The scattering of x-ray photons, which occurs at a time scale much faster than these oscillations, reflects a statistical average of all the distortions distributed across the sample at a given time and, therefore, cannot be used to distinguish it from a random distribution of frozen static distortion, which might still preserve the global cubic symmetry, despite the breaking of the local one. On the contrary, the static version of the JT effect can be reasonably argued against using several lines of reasoning (see Fig. 5 for details). First, there is a clear signature of order-parameter-like increase of intensity associated with charge quadrupolar order composed of two components, an antiferro $\mathcal{T}_x$ and a ferro $\mathcal{T}_z$[27,49]. Concomitantly, it is observed that oxygen ions move away from their high-symmetry positions accordingly, reflecting a strong coupling between local distortions and $\mathcal{T}_z$ charge quadrupoles[30,50]. Those distortions are, however, 5 times smaller than calculated for the Jahn-Teller effect, and of an opposite sign. The frozen landscape of static JT distortions would inevitably lead to a glassy behavior of a charge quadrupolar and magnetic dipole orders since the direction of

magnetic dipoles below T_Q is determined by the local orientation of $\mathcal{T}_z$ quadrupolar moments[50].

The second argument for the dynamic JT state is related to the local symmetry of Re ions. As has been demonstrated in ^{23}Na NMR experiments on Ba_2NaOsO_6, a single resonance line at high temperatures splits into three lines below T_Q, indicating a lowering of the local symmetry[31]. This has been associated with changes in local charge distribution around Na ions, which are surrounded by six OsO_6 octahedra and, therefore, directly reflect shifts of oxygen equilibrium positions. Since the time scale of NMR experiments is much longer than t_0, in the dynamic JT scenario, the local symmetry breaks only below T_Q, while in the static scenario, the triplet line would have been observed at all temperatures, which is in clear contradiction with experimental results[31]. We note that the deformation due to the JT effect is significantly larger than what occurs below T_Q, therefore the splitting of the NMR line would have been clearly seen.

Finally, an argument against the random distribution of locally deformed octahedra comes from the consideration of the effect on the local crystal environment. As revealed by high-resolution synchrotron experiments[27], below T_Q the equilibrium of apical oxygen ions shifts by ~ + 0.36 %, accompanied by a unit cell tetragonal elongation of ~ + 0.15 %. Within the static JT scenario, the random orientation of local distortions would lead to a significant local strain on the surrounding cage of eight Ba ions (almost 1 % of local compression) in order to maintain the observed high-symmetry, cubic unit cell environment above T_Q. Since the quadrupolar moments are randomly frozen, and with such a high lattice strain, there is a clear lack of a feasible mechanism which would lead to the observed coherent distortions below T_Q along the c-axis for both apical oxygen ions and the unit cell as a whole. In addition, if the local distortions are static, the system could remove the strain by lowering the unit cell symmetry from cubic to tetragonal, which is the scenario observed in a series of JT-active d^9 double perovskites $A_2CuB'O_6$ ($A =$ Ba, Sr; $B' =$ W, Te)[51].

The dynamic JT effect ensures the local and global cubic symmetry above T_Q, in accordance with experimental observations in both Ba_2MgReO_6[27] and Ba_2NaOsO_6[31], as well as with ab initio results reported for Ba_2NaOsO_6[52]. Without the shared ligand between ReO_6 octahedra, a feature characteristic for double perovskites, the dynamic distortions on one cluster are not correlated with its neighbors. Following the development of the charge quadrupolar order, where a coherent charge redistribution occurs on Re ions, the PES becomes slightly renormalized, which leads to a slight, but coherent shift of the equilibrium position of oxygen ions, giving rise to the signal observed in REXS experiments[27,49]. Crucially, the dynamic state of ReO_6 octahedra continues to dominate the local Re environment even within the multi-polar ordered state. Even with a complete model of spin-orbit-vibronic coupling, the qualitative picture remains the same[34].

The revelation that the ground-state doublet dominates the low-temperature physics in this class of materials establishes a new paradigm from the thermodynamic point of view. With two phase transitions and two order parameters, it is puzzling how to reconcile $R2$ across both T_M and T_Q. Concurrently, specific heat at T_Q does not exhibit a typical λ-type profile, and, as we have shown, no lifting of degeneracy accompanies the quadrupolar order. Some of the entropy (~ 1/3$R2$) is released above T_M, pointing to a reduction from a three-dimensional towards a two-dimensional phase space for fluctuating magnetic moments[50]. The plane of fluctuation below T_Q is then dictated by the orientation of quadrupolar moments $\mathcal{T}_x$ and $\mathcal{T}_z$, being perpendicular to the $\mathcal{T}_z$-induced elongation. At T_M the directional locking within that plane leads to magnetic dipole order and removes the remaining entropy. We infer that the magnetic and quadrupolar order parameters are part of a single, entangled object that goes through a two-step transition[53].
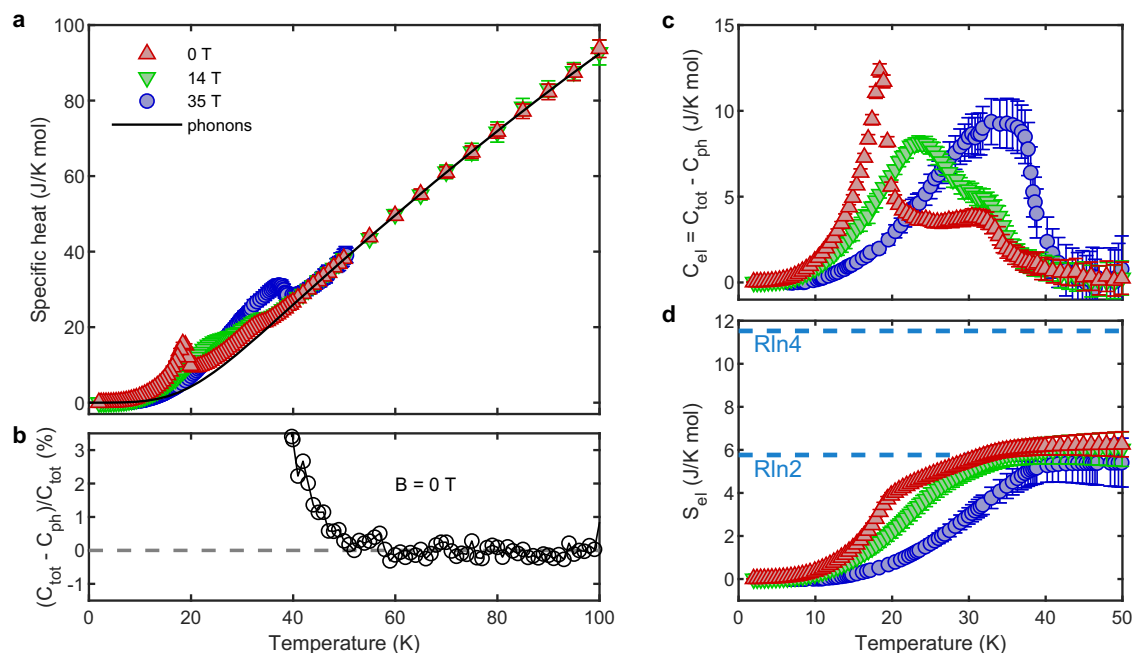
Fig. 4 | Specific heat measurements of Ba$_2$MgReO$_6$. a T-dependence of the total specific heat of Ba$_2$MgReO$_6$. **b** The relative error of the electronic specific heat after the phonon background subtraction. **c** T-dependence of the electronic specific heat in various magnetic fields. **d** T-dependence of recovered entropy. The error bars in Panel (**a**) are obtained during the measurement as a result of the fitting procedure. The error bars in panels (**c**) and (**d**) are calculated based on errors in Panel (**a**).
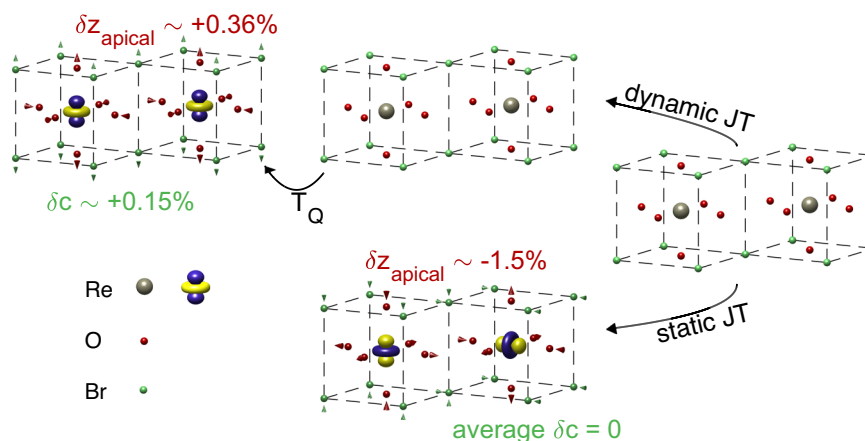
Fig. 5 | Comparison of dynamic and static JT effect on equilibrium ion positions at time-scales longer than t_0. At very high temperatures, the octahedra are not distorted, and the ground state is four-fold degenerate. In the dynamical JT scenario, the degeneracy is lowered by a contraction of Re - O distances (~ − 1.5 %) on time scales $t < t_0$, but the equilibrium positions of ions at $t > t_0$ do not change significantly, with the Re charge distribution remaining spherical (gray circle). At much lower temperatures ($T < T_Q$), a quadrupolar order sets in, including the ferroic $\mathcal{T}_z$ (blue - increased charge density, yellow - decreased charge density), which is accompanied by a coherent shift of apical oxygen ions (red arrows), leading to a small c-axis elongation (~ + 0.15 %)[27] (green arrows). In the static JT scenario, each octahedron is locally distorted, with an equal distribution of elongations along three principal axes. This implies a random distribution of $\mathcal{T}_z$ quadrupolar moments and a lack of coherent ordering at low temperatures. The local Ba cage is also distorted, leading to the accumulation of lattice strain.

Spin-orbit entanglement plays another crucial role that relates to the dynamical state of ReO$_6$ octahedra. In the weak SOC limit, the available states forming a Mexican hat potential are composed of purely orbital contributions, each state allowing for two spin projections. For the strong SOC case involving $5d$ orbitals, the entanglement entails a varying spin projection along the degeneracy line, resulting in a dynamically renormalized directional coupling between neighboring ReO$_6$ octahedra. Similar to Kitaev physics[21], and aided by the frustration on an FCC lattice, it could be envisaged that such a renormalization could lead to a spin-liquid state or other exotic quantum phases.

Methods

Sample preparation

Single crystals were grown by the flux method. A stoichiometric mixture of BaO, MgO, and ReO3 powders was mixed with a flux composed of 36 wt % BaCl2 and 64 wt % MgCl2 in an argon-filled glove box. The mixture was sealed in a platinum tube of 20 mm length and 6 mm diameter. The tube was heated at 1300 ^{0}C and then slowly cooled to 900 ^{0}C at a rate of 5 ^{0}C/h, followed by furnace cooling to room temperature. After the residual flux was washed away with distilled water, several crystals were obtained, The crystals exhibit octahedral morphology, forming flat triangles along [111] and

equivalent directions. Specific heat measurements up to 14 T were performed on as-grown crystals (up to 1 mm in size), while the $B = 35$ T experiment was performed on a 0.3 mm polished crystal. For the Re L_3 edge RIXS experiment the sample was glued on a copper sample holder with the [111] direction perpendicular to the surface. An in situ cleaving has been utilized for the O K edge RIXS experiment.

Resonant inelastic x-ray scattering

The experiments at the Re L_3 edge were performed at BL11XU of SPring-8, Japan synchrotron facility. Incident x-rays were monochromatized by a Si(111) double-crystal monochromator and a two-bounce channel-cut monochromator Si(444), and π-polarized x-rays were irradiated on the samples. Horizontally scattered photons were energy-analyzed by a Ge(733) analyzer. The total energy resolution was 140 meV (full width at half maximum). The experiments at the O K edge were performed at the ADRESS beamline of the Swiss light source (SLS) at the Paul Scherrer Institute (PSI), Switzerland in both the normal and grazing configuration with 50° between incoming and outgoing beams[54].

Embedding quantum chemistry calculations

Many-body wavefunction calculations on electrostatically embedded finite-size clusters were performed using the Molpro package[55]. The model involved a 21-atom cluster consisting of the ReO_6 octahedron together with the nearest 6 Mg and 8 Ba atoms. Re atoms were represented with core potentials and triple-zeta plus two polarization f-functions basis functions[56]. All-electron triple-zeta basis functions were used for O atoms[57]. Both Mg and Ba atoms in the cluster were described by effective core potential and supplemented with a single s basis function[58]. The effect of the crystal lattice surrounding the cluster was treated at the level of Madelung ionic potential, as described in ref. [59]. For the complete active space self-consistent field (CASSCF) calculations, an active space of 3 t_{2g} + 2, e_g orbitals, was used. The optimization was carried out for an average of 5 states, each of unit weight, of the scalar relativistic Hamiltonian. Multireference configuration interaction (MRCI) treatment was performed with single and double substitutions with respect to the CASSCF reference, as described in refs. [60],[61]. The spin-orbit coupling correction was added as described in ref. [62]. The PES was mapped out with respect to isotropic mode $Q_{iso} = (x_1 - x_2 + y_3 - y_4 + z_5 - z_6)$, and e_g-type distortions $Q_2 = (-x_1 + x_2 + y_3 - y_4)$ and $Q_3 = (-x_1 + x_2 - y_3 + y_4 + 2z_5 - 2z_6)$, with superscripts 1,2 referring to the x-axis O atoms, 3,4 to the y-axis O atoms and 5,6 to the z-axis O atoms.

In order to assess the PES, calculations were performed on a grid that varies isotropic distortions were varied from 0.5% to -1.5% with 0.5% steps, with amplitudes referring to non-normalized $Q_{iso} = [1, 1, 1]$ and the percentage being relative to the undistorted 1.926 Å Re − O interatomic distance. A 60° sector of the $Q_2 - Q_3$ plane was simulated, with the angle being varied with steps of 15° and radius being varied from 0 to 3.5%, with the step of 0.25%, with amplitudes referring to normalized $Q_2 = \frac{1}{\sqrt{2}}[-1,1,0]$ and $Q_3 = \frac{1}{\sqrt{6}}[1,1,-2]$. The stability of the minimum with respect to the t_{2g}-type distortions $Q_4 = (y_1 - y_2 + x_3 - x_4)$ was confirmed. In addition, an attempt was made to find a minimum with a non-zero amplitude of the t_{2g}-type distortions by alternating Q_{iso}, Q_2, Q_3, and Q_4 as energy optimization coordinates, starting at the cubic configuration. No such minimum was found, with all paths considered converging back to the minimum described in the article.

Specific heat

For magnetic fields up to 14 T we used a PPMS system (Quantum Design) that utilizes a relaxation method. The measurement at 35 T was performed at LNCMI, Grenoble, France using a Cernox thermometer as a platform and a semi-adiabatic method. In both cases the addenda has been measured separately and subtracted to obtain specific heat of the sample. Zero-field measurements have been used to normalize the results from two setups.

Data availability

All the data that support the findings of this study are available in the Zenodo repository (https://zenodo.org/doi/10.5281/zenodo.13765588).

Code availability

The code for calculations presented in this study is available from the corresponding author upon request.

References

1. Bersuker, I. *The Jahn-Teller Effect* (Cambridge University Press, 2006).
2. Li, M. et al. Ultrafast imaging of spontaneous symmetry breaking in a photoionized molecular system. *Nat. Commun.* **12**, 4233 (2021).
3. Ridente, E. et al. Femtosecond symmetry breaking and coherent relaxation of methane cations via x-ray spectroscopy. *Science* **380**, 713 (2023).
4. Barlow, K. et al. Photoinduced Jahn-Teller switch in Mn(iii) terpyridine complexes. *Dalton Trans.* **51**, 10751 (2022).
5. Babar, R. & Kabir, M. Gate-dependent vacancy diffusion in graphene. *Phys. Rev. B* **98**, 075439 (2018).
6. Keller, H., Bussmann-Holder, A. & Müller, K. A. Jahn-Teller physics and high-Tc superconductivity. *Materials Today* **11**, 38 (2008).
7. Zheng, R. K. et al. The role of the cooperative Jahn-Teller effect in the charge-ordered La$_{1-x}$Ca$_x$MnO3(0.5x0.87) manganites. *Appl. Phys. Lett.* **83**, 5250 (2003).
8. Vitalone, R. A. et al. Nanoscale femtosecond dynamics of mott insulator (Ca$_{0.99}$Sr$_{0.01}$)$_2$RuO$_4$. *Nano Lett.* **22**, 5689 (2022).
9. Geirhos, K. et al. Cooperative cluster jahn-teller effect as a possible route to antiferroelectricity. *Phys. Rev. Lett.* **126**, 187601 (2021).
10. Khomskii, D. I. & Streltsov, S. V. Orbital effects in solids: basics, recent progress, and opportunities. *Chem. Rev.* **121**, 2992 (2021).
11. Millis, A. J., Shraiman, B. I. & Mueller, R. Dynamic Jahn-Teller effect and colossal magnetoresistance in La$_{1-x}$Sr$_x$MnO3. *Phys. Rev. Lett.* **77**, 175 (1996).
12. Kayanuma, Y. & Nakamura, K. G. Dynamic Jahn-Teller viewpoint for generation mechanism of asymmetric modes of coherent phonons. *Phys. Rev. B* **95**, 104302 (2017).
13. Ribeiro, R. F. & Yuen-Zhou, J. Continuous vibronic symmetries in Jahn-Teller models. *J. Phys. Condens. Matter* **30**, 333001 (2018).
14. Klupp, G. et al. Dynamic Jahn–Teller effect in the parent insulating state of the molecular superconductor Cs$_3$C$_{60}$. *Nat. Commun.* **3**, 912 (2012).
15. Iwahara, N. & Chibotaru, L. F. Dynamical Jahn-Teller effect and antiferromagnetism in Cs$_3$C$_{60}$. *Phys. Rev. Lett.* **111**, 056401 (2013).
16. Zadik, R. H. et al. Optimized unconventional superconductivity in a molecular Jahn-Teller metal. *Sci. Adv.* **1**, e1500059 (2015).
17. Wieczorek, K. et al. Electrostrictive and piezoelectric effect in BaTiO3 and PbZrO3. *Ferroelectrics* **336**, 61 (2006).
18. Bersuker, I. B. Giant permittivity and electrostriction induced by dynamic Jahn-Teller and pseudo Jahn-Teller effects. *Appl. Phys. Lett.* **107**, 202904 (2015).
19. Hasan, M. Z. & Kane, C. L. Colloquium: Topological insulators. *Rev. Mod. Phys.* **82**, 3045 (2010).
20. Armitage, N. P., Mele, E. J. & Vishwanath, A. Weyl and Dirac semimetals in three-dimensional solids. *Rev. Mod. Phys.* **90**, 015001 (2018).
21. Takagi, H., Takayama, T., Jackeli, G., Khaliullin, G. & Nagler, S. E. Concept and realization of Kitaev quantum spin liquids. *Nat. Rev. Phys.* **1**, 264 (2019).
22. Plotnikova, E. M., Daghofer, M., van den Brink, J. & Wohlfeld, K. Jahn-Teller effect in systems with strong on-site spin-orbit coupling. *Phys. Rev. Lett.* **116**, 106401 (2016).

23. Liu, H. & Khaliullin, G. Pseudo-Jahn-Teller effect and magnetoelastic coupling in spin-orbit mott insulators. *Phys. Rev. Lett.* **122**, 057203 (2019).

24. Boothroyd, A. T. et al. Localized 4f states and dynamic jahn-teller effect in pro₂. *Phys. Rev. Lett.* **86**, 2082 (2001).

25. Streltsov, S. V. & Khomskii, D. I. Jahn-Teller effect and spin-orbit coupling: Friends or foes? *Phys. Rev. X* **10**, 031043 (2020).

26. Hirai, D. & Hiroi, Z. Successive symmetry breaking in a Jeff = 3/2 quartet in the spin-orbit coupled insulator Ba_2MgReO_6. *J. Phys. Soc. Jpn.* **88**, 064712 (2019).

27. Hirai, D. et al. Detection of multipolar orders in the spin-orbit-coupled 5d Mott insulator Ba_2MgReO_6. *Phys. Rev. Res.* **2**, 022063 (2020).

28. Frontini, F. I. et al. Spin-Orbit-Lattice Entangled State in A_2MgReO_6 (A = Ca, Sr, Ba) Revealed by Resonant Inelastic x-Ray Scattering. *Phys. Rev. Lett.* **133**, 036501 (2024).

29. Agrestini, S. et al. Origin of magnetism in a supposedly non-magnetic osmium oxide. *Phys. Rev. Lett.* **133**, 066501 (2024).

30. Chen, G., Pereira, R. & Balents, L. Exotic phases induced by strong spin-orbit coupling in ordered double perovskites. *Phys. Rev. B* **82**, 174440 (2010).

31. Lu, L. et al. Magnetism and local symmetry breaking in a Mott insulator with strong spin orbit interactions. *Nat. Commun.* **8**, 14407 (2017).

32. Xu, L. et al. Covalency and vibronic couplings make a nonmagnetic j=3/2 ion magnetic. *Npj Quantum Mater.* **1**, 16029 (2016).

33. Svoboda, C., Zhang, W., Randeria, M. & Trivedi, N. Orbital order drives magnetic order in 5d¹ and 5d² double perovskite Mott insulators. *Phys. Rev. B* **104**, 024437 (2021).

34. Iwahara, N. & Chibotaru, L. F. Vibronic order and emergent magnetism in cubic d¹ double perovskites. *Phys. Rev. B* **107**, L220404 (2023).

35. Razavy, M. *Quantum Theory of Tunneling*, 2nd ed. (World Scientific, 2014).

36. Erickson, A. S. et al. Ferromagnetism in the mott insulator Ba_2NaOsO_6. *Phys. Rev. Lett.* **99**, 016404 (2007).

37. Willa, K. et al. Phase transition preceding magnetic long-range order in the double perovskite Ba_2NaOsO_6. *Phys. Rev. B* **100**, 041108 (2019).

38. Ishikawa, H. et al. Ordering of hidden multipoles in spin-orbit entangled 5d¹ Ta chlorides. *Phys. Rev. B* **100**, 045142 (2019).

39. Mansouri Tehrani, A. et al. Charge multipole correlations and order in cs₂Tacl₆. *Phys. Rev. Res.* **5**, L012010 (2023).

40. Maharaj, D. D. et al. Octupolar versus néel order in cubic 5d² double perovskites. *Phys. Rev. Lett.* **124**, 087206 (2020).

41. Kermarrec, E. et al. Frustrated fcc antiferromagnet Ba_2YOsO_6: Structural characterization, magnetic properties, and neutron scattering studies. *Phys. Rev. B* **91**, 075133 (2015).

42. Marjerrison, C. A. et al. Cubic Re6+ (5d1) double perovskites, Ba2MgReO6, Ba2ZnReO6, and Ba2Y2/3ReO6: Magnetism, heat capacity, uSR, and neutron scattering studies and comparison with theory. *Inorg. Chem.* **55**, 10701 (2016).

43. Ishikawa, H. et al. Phase transition in the 5d¹ double perovskite Ba_2CaReO_6 induced by high magnetic field. *Phys. Rev. B* **104**, 174422 (2021).

44. Pásztorová, J., Tehrani, A. M., Živković, I., Spaldin, N. A. & Rønnow, H. M. Experimental and theoretical thermodynamic studies in Ba2MgReO6—the ground state in the context of Jahn-Teller effect. *J. Phys. Condens. Matter* **35**, 245603 (2023).

45. Peysson, Y., Ayache, C., Rossat-Mignod, J., Kunii, S. & Kasuya, T. High magnetic field study of the specific heat of CeB₆ and LaB₆. *J. Phys. France* **47**, 113 (1986).

46. Amara, M. Dynamical splitting of cubic crystal field levels in rare-earth cage compounds. *Phys. Rev. B* **99**, 174405 (2019).

47. Shiina, R., Shiba, H. & Thalmeier, P. Magnetic-field effects on quadrupolar ordering in a Γ_8-quartet system CeB₆. *J. Phys. Soc. Jpn.* **66**, 1741 (1997).

48. Matsumura, T., Yonemura, T., Kunimori, K., Sera, M. & Iga, F. Magnetic field induced 4f octupole in CeB₆ probed by resonant X-ray diffraction. *Phys. Rev. Lett.* **103**, 017203 (2009).

49. Soh, J.-R. et al. Spectroscopic signatures and origin of a hidden order in Ba_2MgReO_6. Preprint at https://doi.org/10.48550/arXiv.2312.01767 (2023).

50. Mansouri Tehrani, A. & Spaldin, N. A. Untangling the structural, magnetic dipole, and charge multipolar orders in Ba_2MgReO_6. *Phys. Rev. Mater.* **5**, 104410 (2021).

51. Iwanaga, D., Inaguma, Y. & Itoh, M. Crystal structure and magnetic properties of b-site ordered perovskite-type oxides a2cubo6 (a=ba, sr; b=w, te). *J. Solid State Chem.* **147**, 291 (1999).

52. Iwahara, N., Vieru, V. & Chibotaru, L. F. Spin-orbital-lattice entangled states in cubic d¹ double perovskites. *Phys. Rev. B* **98**, 075138 (2018).

53. Lovesey, S. W. & Khalyavin, D. D. Magnetic order and 5d¹ multipoles in a rhenate double perovskite ba2mgreo6. *Phys. Rev. B* **103**, 235160 (2021).

54. Strocov, V. et al. High-resolution soft x-ray beamline adress at the swiss light source for resonant inelastic x-ray scattering and angle-resolved photoelectron spectroscopies. *J. Synchrotron Radiat.* **17**, 631 (2010).

55. Werner, H.-J., Knowles, P. J., Knizia, G., Manby, F. R. & Schuetz, M. Molpro: a general-purpose quantum chemistry program package. *Wiley Interdiscip. Rev. Comput. Mol. Sci.* **2**, 242 (2012).

56. Figgen, D., Peterson, K. A., Dolg, M. & Stoll, H. Energy-consistent pseudopotentials and correlation consistent basis sets for the 5d elements Hf-Pt. *J. Chem. Phys.* **130**, 164108 (2009).

57. Peterson, K. A. & Dunning Jr, T. H. Accurate correlation consistent basis sets for molecular core-valence correlation effects: The second row atoms Al-Ar, and the first row atoms B-Ne revisited. *J. Chem. Phys.* **117**, 10548 (2002).

58. Fuentealba, P., von Szentpaly, L., Preuss, H. & Stoll, H. Pseudopotential calculations for alkaline-earth atoms. *J. Phys. B Atom. Mol. Phys.* **18**, 1287 (1985).

59. Klintenberg, M., Derenzo, S. & Weber, M. Accurate crystal fields for embedded cluster calculations. *Comput. Phys. Commun.* **131**, 120 (2000).

60. Knowles, P. J. & Werner, H.-J. Internally contracted multiconfiguration-reference configuration interaction calculations for excited states. *Theor. Chim. Acta* **84**, 95 (1992).

61. Werner, H. & Knowles, P. J. An efficient internally contracted multiconfiguration-reference configuration interaction method. *J. Chem. Phys.* **89**, 5803 (1988).

62. Berning, A., Schweizer, M., Werner, H.-J., Knowles, P. J. & Palmieri, P. Spin-orbit matrix elements for internally contracted multireference configuration interaction wavefunctions. *Mol. Phys.* **98**, 1823 (2000).

Acknowledgements

Author contributions

Single crystals were grown by D.H., D.T., and J.P. RIXS data was measured and analyzed by I.Ž., J-R.S., F.P., K.I., Y.W., W.Z., C.G., T.Y., T.S., and H.M.R. Embedding quantum chemistry calculations were performed by O.M. and R.Y. under guidance of O.V.Y. and H.M.R. Specific heat was measured and analyzed by I.Ž. and A.D. The phonon contribution to specific heat was calculated by A.M.T. The manuscript was written by I.Ž. with contributions from all co-authors.

Competing interests

The authors declare no competing interests.

Additional information

Correspondence and requests for materials should be addressed to Ivica Živković.

Publisher's note Springer Nature remains neutral with regard to jurisdictional claims in published maps and institutional affiliations.